RSC Advances

PAPER

View Article Online
View Journal | View Issue

Cite this: *RSC Adv.*, 2025, **15**, 8354

Detection of an oxidative stress metabolite associated with neurodegenerative diseases: effect of heteroatom doped antioxidant carbon dots†

Mohammad Tabish, *[ab] Iram Malik, [cb] Abdulrahman M. Alshahrani [d] and Mohd Afzal *[e]

Carbon dots (CDs) are neoteric forms of carbon nanostructures, and play a fundamental role in early diagnosis and controlling of neurological disorders (NDs). Aiming towards the detection of an oxidative stress metabolite, the present study provides an innovative strategy for developing heteroatom-doped carbon dots using tamarind as a sustainable carbon source and urea as a nitrogen dopant through a one-step hydrothermal process. This method offers a cost-effective and eco-friendly solution without compromising performance. The structural and functional properties of the synthesized CDs were characterized using advanced techniques, including fluorescence spectroscopy, UV-visible spectroscopy, Fourier transform infrared (FTIR) spectroscopy, and X-ray photoelectron spectroscopy (XPS). Antioxidant assessments revealed remarkable free-radical scavenging activity (exceeding 80% efficiency) across three independent methodologies. Furthermore, the CDs demonstrated exceptional sensitivity and selectivity in detecting oxidative stress metabolites, particularly 3-nitrotyrosine, with detection efficiency influenced by environmental pH (4.8–8.7). Biocompatibility studies using fibroblast cells confirmed their non-toxic nature, supporting their potential for biomedical applications. Collectively, these findings highlight the promise of heteroatom-doped CDs as a novel platform for detecting oxidative stress metabolites associated with neurodegenerative diseases, bridging fundamental research with real-world diagnostic advancements.

Received 11th January 2025
Accepted 8th March 2025

DOI: 10.1039/d5ra00274e

rsc.li/rsc-advances

1. Introduction

Neurodegenerative disorders can lead to a gradual deterioration of the nerve structures essential for normal brain functions and are recognized as a major public health problem, particularly in the developing world.[1] The reason behind this neurological disability arises due to some genetic changes induced by environmental factors and oxidative stress.[2,3] Oxidative stress, defined as an imbalance between the generation of reactive oxygen species (ROS) and antioxidant defenses, is a defining feature of various neurodegenerative disorders, such as Alzheimer's disease (AD), Parkinson's disease (PD), and Huntington's disease (HD).[4] These disorders, frequently progressive and irreversible, entail the slow degradation of neurons, compromising cognitive and motor skills.[5] The buildup of oxidative stress metabolites, including malondialdehyde, 4-hydroxynonenal, and other aldehydes, intensifies neuronal injury, establishing a detrimental loop of cellular impairment.[6] Oxidative stress is a condition characterized by an imbalance between the production of ROS and the biological system's ability to neutralize those using antioxidants. ROS, such as superoxide radicals (O_2^{-}), hydrogen peroxide (H_2O_2), and hydroxyl radicals ($^{\bullet}OH$), are naturally generated as byproducts of cellular metabolism.[7] While ROS play critical roles in cell signaling, immune responses, and homeostasis, excessive accumulation leads to oxidative damage of proteins, lipids, and DNA, contributing to various pathological conditions, including neurodegenerative diseases.[8] In neurodegenerative disorders such as Alzheimer's and Parkinson's disease, elevated ROS levels trigger oxidative stress, promoting neuronal damage and disease progression.[9] The detection of oxidative stress biomarkers, such as 3-nitrotyrosine (3NT), is therefore crucial for understanding disease mechanisms and developing diagnostic tools. Timely and precise identification of these metabolites is essential for comprehending illness development and formulating treatment approaches.

[a]*Department of Pharmacology, College of Medicine, Shaqra University, Shaqra 11961, Saudi Arabia. E-mail: tabish@su.edu.sa*

[b]*King Salman Center for Disability Research, Riyadh 11614, Saudi Arabia*

[c]*Department of Electrical Engineering, College of Engineering, Prince Sattam Bin Abdulaziz University, Al-Kharj, 11942, Saudi Arabia*

[d]*Department of Internal Medicine (Neurology), College of Medicine, Shaqra University, Shaqra, 11961, Saudi Arabia*

[e]*Department of Chemistry, College of Science, King Saud University, Riyadh, 11451, Saudi Arabia. E-mail: maslam1@ksu.edu.sa*

† Electronic supplementary information (ESI) available. See DOI: https://doi.org/10.1039/d5ra00274e

In past few years, researchers have been focused on the creation of nanotechnology system that can be implication in a variety of medical sectors.[10] In this context, nanomaterials have emerged as transformative instruments due to their distinctive capacity to engage with biological systems at the molecular level.[11–13] Their nanoscale dimensions enable entry into cellular and subcellular settings, while their adjustable surface chemistry permits targeted interactions with biomarkers linked to neurodegeneration.[14] Among nanomaterials, CDs emerge as a suitable platform for the investigation of neurodegenerative diseases.[15]

Carbon dots (CDs), a category of fluorescent carbon-based nanomaterials, have attracted considerable interest owing to their remarkable physicochemical characteristics, such as adjustable fluorescence, superior photostability, biocompatibility, and little toxicity.[16,17] Derived from sustainable and economical predecessors, these nanostructures provide a diverse substrate for various applications, especially in sensing.[18–20] The nanoscale size of CDs confers a substantial surface area, offering several reactive sites for functionalization with certain chemical groups.[21–23] This distinctive characteristic improves their capacity to selectively engage with target molecules, rendering CDs exceptionally efficient as sensors.[24–26] Moreover, their fluorescence response is responsive to environmental variations, including pH, redox conditions, and particular metabolite concentrations, facilitating accurate identification.[27–29] The incorporation of heteroatoms, such nitrogen, sulfur, or phosphorus, during synthesis enhances their electronic characteristics, increasing sensitivity and selectivity.[30–34] As a result, heteroatom-doped carbon dots have become strong contenders for the detection of biomolecules and metabolites associated with oxidative stress, particularly those involved in significant clinical disorders.[35]

The antioxidant characteristics of CDs, especially those infused with heteroatoms, allow them to efficiently neutralize ROS, hence reducing oxidative harm in biological systems.[36] The dual role of CDs, serving as both antioxidants and sensors, establishes them as a distinctive instrument for tackling the issues associated with neurodegenerative disorders.[37] By combining ROS-scavenging capabilities with sensitive detection techniques, CDs can elucidate the oxidative stress environment of sick neurons.[38] For example, CDs equipped with particular identification elements can identify oxidative stress metabolites, facilitating real-time observation of their concentration and behavior within neuronal contexts.[39–41] These qualities are essential for early detection and comprehension of the fundamental causes of neurodegeneration. Neurodegenerative disorders represent a worldwide health issue, exacerbated by an aging demographic that increases their frequency. Present diagnostic instruments and treatment alternatives are constrained, frequently emphasizing symptomatic relief instead of targeting underlying causes. The utilization of nanomaterials, such as carbon dots, presents a transformative change.[42] Their capacity to traverse the blood–brain barrier, engage with neural tissue, and deliver targeted therapeutic and diagnostic activities renders them essential for the progression of neurodegenerative research.[43] CDs, due to their biocompatibility and multifunctionality, are ideally suited for brain applications. Their fluorescent characteristics provide non-invasive imaging, while their surface chemistry permits conjugation with targeted ligands, thereby augmenting selectivity for sick tissue.[44] Furthermore, heteroatom doping enhances their electrical and optical characteristics while also providing catalytic activity, crucial for the detection and neutralization of ROS. Deng *et al.* offered a hypothesis to augment the antioxidant capacity of biomass carbon dots through precursor optimization, extraction solvent selection, and various circumstances, utilizing broccoli as the biomass source.[45] This study demonstrated that the antioxidant efficacy of CDs can be augmented by employing solvent extracts of biomass as precursors. The resultant biomass waste extract-derived carbon dots display attributes of environmental sustainability, minimal toxicity, and superior antioxidant and anti-inflammatory properties, indicating their potential as an effective antioxidant nanomedicine for inflammatory treatment. The suppression of β-amyloid (Aβ) peptide aggregation and the degradation of the Aβ fibril structure by N-CDs were also examined.[46] To construct an ideal nanoscale ROS scavenging agent, another group of researchers has synthesized ten varieties of biocompatible graphene quantum dots (GQDs) enhanced with different metal dopants.[47] Due to their multifunctionality, biocompatible doped GQD antioxidants may serve as promising options for multimodal therapies, encompassing the lowering of reactive oxygen species alongside imaging and medicinal administration to cancer tumors.

Despite significant advancements in carbon dot synthesis and their applications in biomedical sensing, there remains a critical need for a sustainable, cost-effective, and highly selective approach for detecting oxidative stress metabolites linked to neurodegenerative diseases. In this study, we report the synthesis of heteroatom-doped carbon dots (TUCDs) using tamarind as a renewable carbon precursor and urea as a nitrogen dopant *via* a one-step hydrothermal method. Tamarind is a highly sustainable, abundant, and cost-effective natural resource rich in polyphenols, flavonoids, and organic acids, which serve as excellent precursors for carbon dot synthesis. These inherent biomolecules facilitate the formation of graphitic structures and enhance the antioxidant properties of the synthesized CDs. Additionally, tamarind-based CDs exhibit superior photoluminescence, stability, and biocompatibility, making them highly suitable for biomedical applications, particularly in oxidative stress detection. Furthermore, compared to other natural carbon sources, tamarind offers a well-balanced composition of carbonaceous and heteroatom-rich content, making it an ideal candidate for developing heteroatom-doped CDs with enhanced functionality. This approach not only provides an eco-friendly alternative to conventional synthetic methods but also enhances the antioxidant properties and selectivity of the CDs for biomolecular detection. The synthesized CDs exhibit excellent free-radical scavenging activity and demonstrate a high-affinity interaction with 3-nitrotyrosine, a key oxidative stress biomarker, with detection sensitivity modulated by environmental pH. Furthermore, their non-toxic nature, confirmed through biocompatibility studies, reinforces their suitability for

biomedical applications. By integrating sustainability, antioxidant efficiency, and selective metabolite detection, this work presents a promising strategy for developing nanomaterials capable of addressing challenges in neurodegenerative disease diagnostics.

2. Materials and methods

2.1. Materials

The tamarind (*Tamarindus indica*) for CDs synthesis was brought from a local supermarket. Urea and 3-nitro-L-tyrosine (3NT; crystalline) were purchased from Sigma Germany and used as received. Human serum, 2,2′-azinobis (3-ethylbenzothiazoline-6-sulfonic acid) (ABTS) and 2,2-diphenyl-1-picrylhydrazyl (DPPH) were supplied by Sigma-Aldrich (Germany). The 3T3 fibroblast cell line was purchased from ATCC, USA. Sodium hydroxide (NaOH), hydrochloric acid (HCl), sodium chloride (NaCl), sulfuric acid (H_2SO_4), quinine sulfate (QS), and 3-(4,5-dimethylthiazol-2-yl)-2,5-diphenyltetrazolium bromide (MTT) were acquired from Sigma Aldrich. Dimethyl sulfoxide (DMSO) was acquired from Himedia. All other chemicals used were of analytical grade. All studies were conducted using Milli-Q water.

2.1.1 Synthesis of tamarind and urea derived CDs (TUCDs). Nitrogen-doped carbon dots generated from tamarind were synthesized *via* a hydrothermal method, utilizing tamarind as the principal carbon source and urea as the nitrogen dopant. Initially, ripe tamarind pulp was extracted, meticulously cleaned to exclude seeds and contaminants, then dried at 60 °C until a uniform mass was attained. The desiccated tamarind pulp was further pulverized into a paste-like texture. Approximately 5 g of tamarind pulp were combined with 20 mL of deionized water and 1 g of urea in a beaker. The homogeneous mixture was placed in a Teflon-lined stainless-steel autoclave and underwent hydrothermal treatment at 180 °C for 8 h. This technique enabled the carbonization of tamarind pulp and the integration of nitrogen atoms from urea into the carbon structure. Upon cooling the autoclave to ambient temperature, the resulting dark brown dispersion was collected and subjected to centrifugation at 10 000 rpm for 15 minutes to eliminate unreacted particles and big particulates. The supernatant was subsequently filtered *via* a 0.22 μm membrane filter to yield a clear TUCD solution. The TUCDs were further purified by dialyzing the solution in deionized water using a dialysis membrane having a molecular weight cut-off of approximately 1000 Da for 24 h. The synthesized TUCDs demonstrated a homogeneous size distribution, exceptional water dispersibility, and robust fluorescence under UV light. The characteristics resulting from nitrogen doping and the presence of several surface functional groups (including hydroxyl, carboxyl, and amino groups) render TUCDs very appropriate for integration into biopolymer-based packaging materials for diverse applications. Fig. 1 presents a comprehensive schematic of the TUCDs synthesis process, encompassing the essential stages of hydrothermal reaction, centrifugation, dialysis, and lyophilization.

2.2. Detection of 3NT by TUCDs

The detection of 3-nitro-L-tyrosine (3NT) was performed using the synthesized tamarind-derived nitrogen-doped carbon dots (TUCDs). The fluorescence quenching property of the TUCDs in the presence of 3NT was utilized for ultrasensitive and selective detection. To begin, a stock solution of TUCDs was prepared by dispersing the synthesized carbon dots in deionized water to achieve a stable and homogeneous colloidal solution. Separately, a series of standard 3NT solutions with varying concentrations (ranging from nanomolar to micromolar levels) were prepared in phosphate-buffered saline (PBS, pH 7.4). In a typical detection assay, 2 mL of the TUCD solution was mixed with 100 μL of the 3NT solution at a specific concentration. The resulting

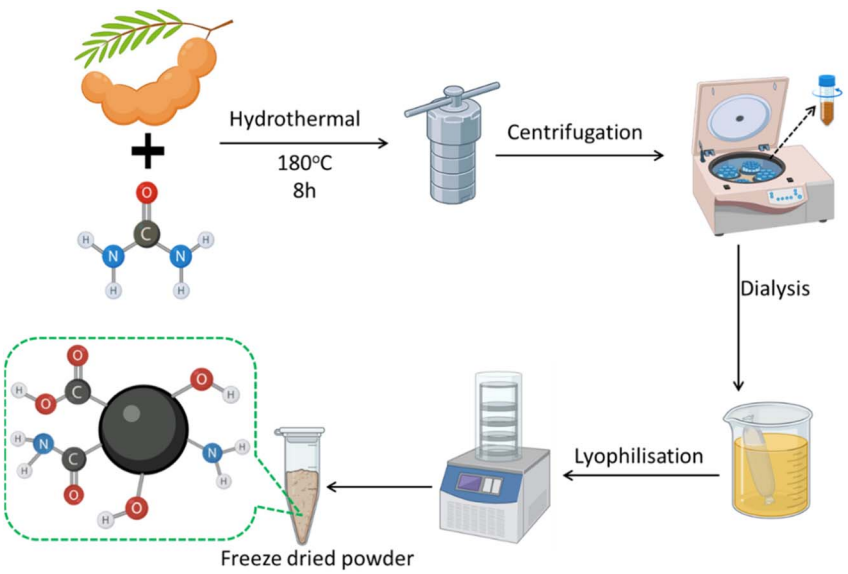

Fig. 1 Schematic representation of synthesis of TUCDs.

mixture was incubated at room temperature for 5 minutes to allow interaction between 3NT and the TUCDs. The fluorescence emission spectra were then recorded using a fluorescence spectrophotometer, with an excitation wavelength of 365 nm. The fluorescence intensity of the TUCDs showed a significant quenching effect in the presence of 3NT due to the formation of a photoinduced electron transfer (PET) system between the electron-donating TUCDs and the electron-accepting nitro group of 3NT. To evaluate the sensitivity of the detection method, the fluorescence quenching efficiency (F_0/F) was plotted against the concentration of 3NT, where F_0 and F represent the fluorescence intensities of the TUCDs in the absence and presence of 3NT, respectively. The detection limit (LOD) was calculated based on the signal-to-noise ratio (S/N = 3). The method demonstrated an excellent linear response over a wide concentration range, with a remarkably low LOD, indicating the ultrasensitive nature of the detection system. For specificity analysis, the fluorescence response of the TUCDs was examined in the presence of other structurally similar compounds, including tyrosine, nitrobenzene, and other nitroaromatic compounds. The TUCDs exhibited negligible fluorescence changes in the presence of these interferents, confirming the high selectivity of the system toward 3NT. To further validate the practical application, the detection of 3NT was conducted in human serum samples. The serum samples were diluted with PBS and spiked with known concentrations of 3NT. The recovery rates of 3NT were calculated, and the results demonstrated high accuracy and reliability, indicating the potential of TUCDs for real-world biological applications.

3. Results and discussions

The synthesis of TUCDs was conducted by a hydrothermal reaction. Tamarind pulp and urea were amalgamated as precursor materials and underwent hydrothermal treatment at 180 °C for 8 hours. The reaction mixture was subsequently centrifuged to exclude big particle contaminants and unreacted precursors. The supernatant acquired post-centrifugation underwent dialysis to purify the TUCDs and eliminate smaller molecular contaminants. Subsequent to dialysis, the fluid was lyophilized to yield a freeze-dried powder of TUCDs. The freeze-dried TUCDs underwent additional analysis for structural and

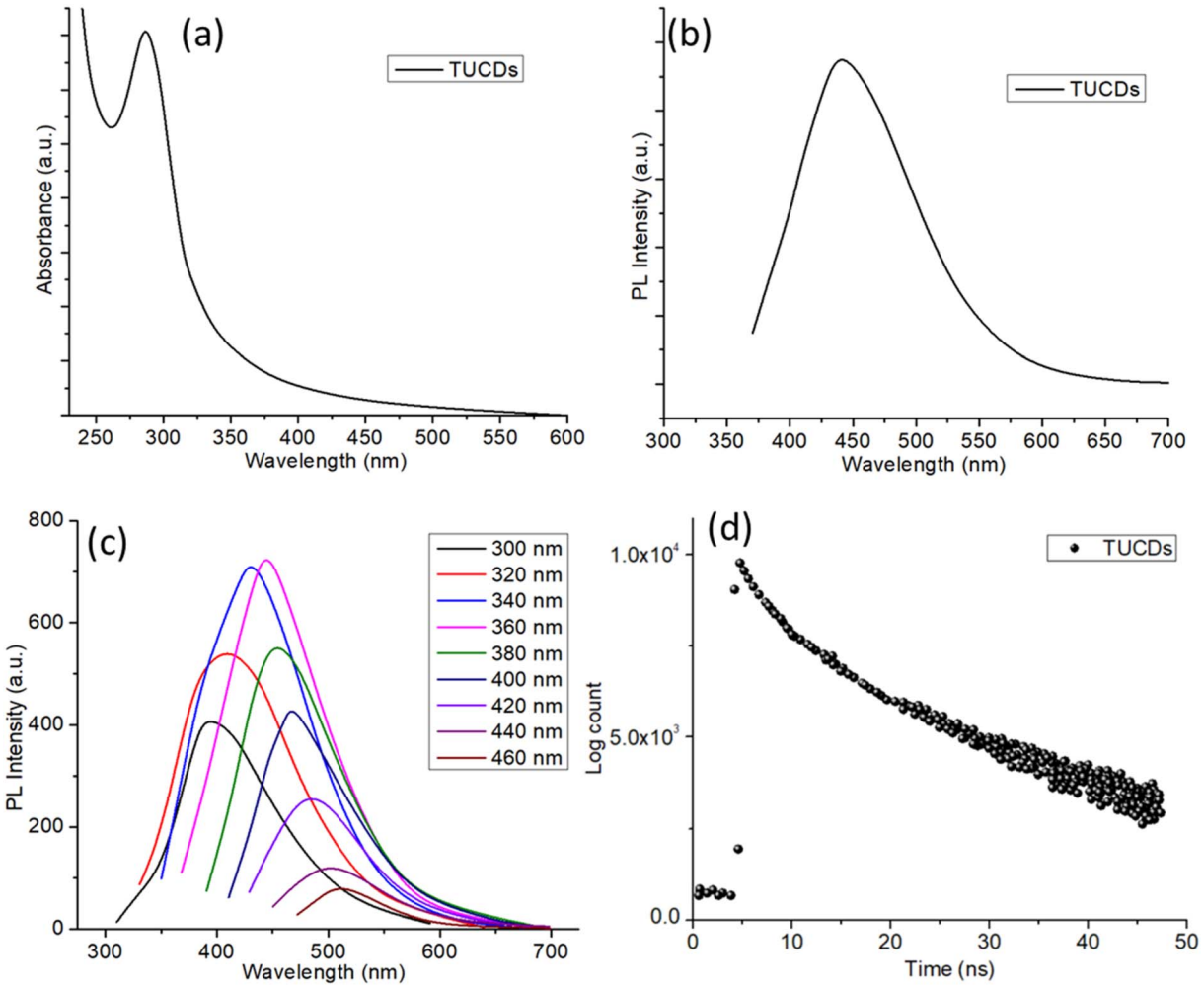

Fig. 2 (a) UV-visible spectrum of TUCDs in aqueous dispersion (b) fluorescence spectrum of the TUCDs (c) excitation dependent fluorescence spectra of the TUCDs (d) lifetime assessment of TUCDs.

functional characterisation. The hydrothermal method, along with subsequent purification procedures, facilitated the generation of high-purity TUCDs, appropriate for prospective uses in. The transmission electron microscopy (TEM) analysis of TUCDs reveals their nanoscale morphology and size distribution, as illustrated in Fig. S1.† The TEM micrograph shows well-dispersed, nearly spherical carbon dots with an average particle size of approximately 3 nm, as determined from the size distribution histogram. The histogram follows a Gaussian distribution, indicating a narrow size distribution, which is critical for achieving uniform optical and electronic properties. The elemental mapping images further confirm the composition of the TUCDs, highlighting the presence of carbon (C), oxygen (O), and nitrogen (N), suggesting successful surface functionalization or doping. The uniform dispersion of these elements supports the formation of oxygen- and nitrogen-rich functional groups, which can enhance the solubility, photoluminescence, and catalytic activity of the TUCDs.

The optical characteristics of the produced TUCDs were assessed using UV-visible absorption spectroscopy, fluorescence spectroscopy, and lifetime measurements, as illustrated in Fig. 2. The UV-visible absorption spectrum of TUCDs (Fig. 2(a)) exhibited a significant peak at around 280 nm. The absorption peak is indicative of the n–π* transitions of C=O or C=N functional groups, possibly formed during the hydrothermal synthesis from the precursors.[48] The results confirm the presence of specific structural characteristics that are essential for the optical activity of TUCDs, as demonstrated by their UV-vis absorption behavior. The fluorescence spectrum of TUCDs (Fig. 2(b)) under 360 nm excitation displayed a pronounced emission peak at around 450 nm, signifying blue fluorescence. The robust emission indicates that the TUCDs exhibit superior photoluminescence characteristics, perhaps attributable to the surface imperfections and functional groups included during synthesis. To investigate the fluorescence characteristics, excitation-dependent emission spectra of TUCDs were obtained (Fig. 2(c)). The emission maxima transitioned from 420 nm to 520 nm as the excitation wavelength rose from 300 nm to 460 nm, signifying excitation-dependent photoluminescence. This behavior is a defining trait of carbon dots and can be ascribed to the heterogeneous nature of the particle surface, quantum size effects, or a combination of emissive traps.[49,50] The excitation-tunable emission increases the applicability of TUCDs in multicolor imaging and sensing. The fluorescence lifetime of TUCDs was assessed to elucidate the decay kinetics (Fig. 2(d)). The decay profile of TUCDs exhibits

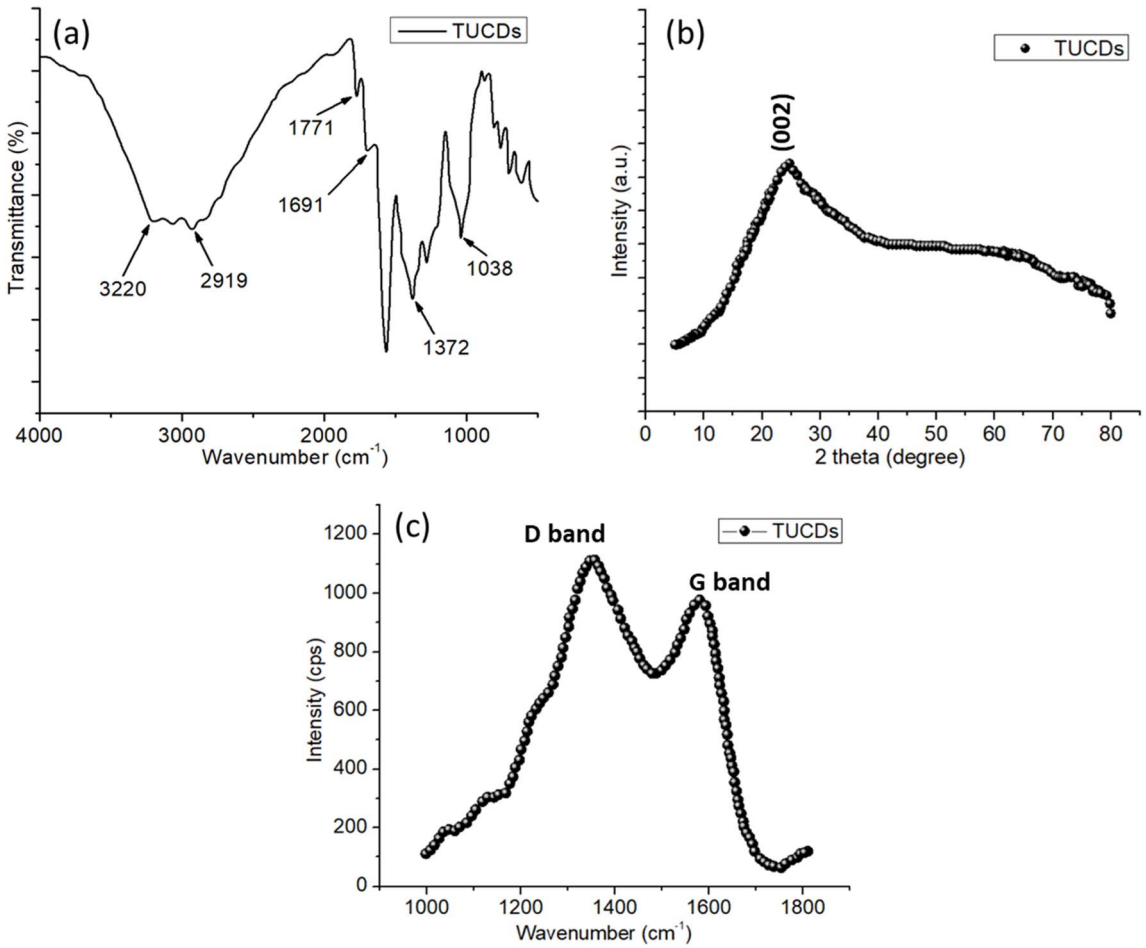

Fig. 3 (a) FTIR spectrum of the TUCDs (b) XRD of the freeze dried TUCDs powder (c) Raman spectrum of the TUCDs.

a multi-exponential nature, indicating the presence of multiple emissive states on their surface. The average fluorescence lifetime, in the nanosecond range, suggests the existence of long-lived emissive states, which is beneficial for applications such as bioimaging, photocatalysis, and optoelectronic devices. Optical characterization further reveals that TUCDs display distinct UV-visible absorption features and excitation-dependent photoluminescence. The combination of fluorescence properties and extended lifetime implies that TUCDs possess a functionalized surface with emissive traps and graphitic cores, making them highly versatile materials. These attributes collectively highlight the potential of TUCDs for applications in biosensing, light-emitting devices, and environmental monitoring. The excitation-dependent emission offers versatility for diverse wavelength-specific applications, demonstrating the adaptability of these nanomaterials.

The structural and chemical properties of the synthesized TUCDs were thoroughly analyzed using FTIR, XRD, and Raman spectroscopy, as presented in Fig. 3. The FTIR spectrum (Fig. 3(a)) reveals the presence of key functional groups that contribute to the chemical versatility of TUCDs. The broad peak at 3220 cm^{-1} corresponds to O–H or N–H stretching vibrations, indicating the presence of hydroxyl or amine groups, which enhance the hydrophilicity of the TUCDs.[51] The peak at 2919 cm^{-1} is assigned to C–H stretching vibrations, suggesting aliphatic hydrocarbons on the surface. A strong absorption band at 1691 cm^{-1} is characteristic of C=O stretching, likely from carboxylic groups, while the peak at 1771 cm^{-1} corresponds to ester or carbonyl groups, further confirming the oxidative nature of the surface chemistry.[52] Peaks at 1372 cm^{-1} and 1038 cm^{-1} correspond to C–N and C–O stretching vibrations, respectively, indicating the presence of amide and ether functionalities. These surface functional groups, formed during the hydrothermal synthesis, enhance the chemical reactivity and provide active sites for interactions,[53] making the TUCDs suitable for applications such as catalysis, drug delivery, and bioimaging.[54–56] The XRD pattern (Fig. 3(b)) confirms the amorphous nature of the TUCDs. A broad diffraction peak centered around $2\theta = 25°$ corresponds to the (002) plane of graphitic carbon. The broadness of this peak suggests a low degree of crystallinity and the presence of disordered carbon structures, likely due to the abundant surface functional groups and lack of a well-ordered graphitic lattice. This amorphous structure is a hallmark of carbon dots and is often associated with excellent optical properties, including fluorescence.[23,57,58] The Raman spectrum (Fig. 3(c)) further highlights the structural characteristics of the TUCDs. Two prominent peaks were observed: the D-band at approximately 1350 cm^{-1}, which is attributed to defects and disordered carbon in the structure, and the G-band at around 1580 cm^{-1}, corresponding to sp^2-hybridized graphitic carbon.[59] The intensity ratio of the D-band to the G-band (I_D/I_G) provides valuable insight into the structural integrity and defect density of the TUCDs. A higher I_D/I_G ratio indicates a significant level of structural defects and disorder, which is consistent with the amorphous nature observed in the XRD pattern. In our study, the I_D/I_G ratio for TUCDs was determined to be ~1.20, suggesting a high degree of structural disorder due to nitrogen incorporation. This result is consistent with other nitrogen-doped carbon dots reported in the literature.[60] These defects, along with the functional groups identified in the FTIR spectrum, play a crucial role in the photoluminescence properties of TUCDs, making them excitation-dependent and highly tunable for diverse applications.

Fig. 4 displays the DLS and zeta potential studies, providing essential information regarding the size distribution and surface charge of the synthesized thermally treated TUCDs in an aqueous environment. Fig. 4(a) displays the DLS spectrum, indicating a monodisperse particle size distribution, with a prominent peak about 100 nm, implying the presence of uniformly dispersed carbon dots with minimal aggregation. This uniform size distribution is crucial for ensuring consistent physicochemical and biological properties, making TUCDs ideal candidates for various biomedical applications, such as drug delivery and bioimaging. Fig. 4(b) depicts the zeta potential measurement, indicating a sharp peak at approximately +35 mV, which reflects a highly positive surface charge on the TUCDs. This high zeta potential value demonstrates the excellent colloidal stability of the particles due to electrostatic repulsion, preventing aggregation in an aqueous environment. Moreover, the positive charge is attributed to the successful

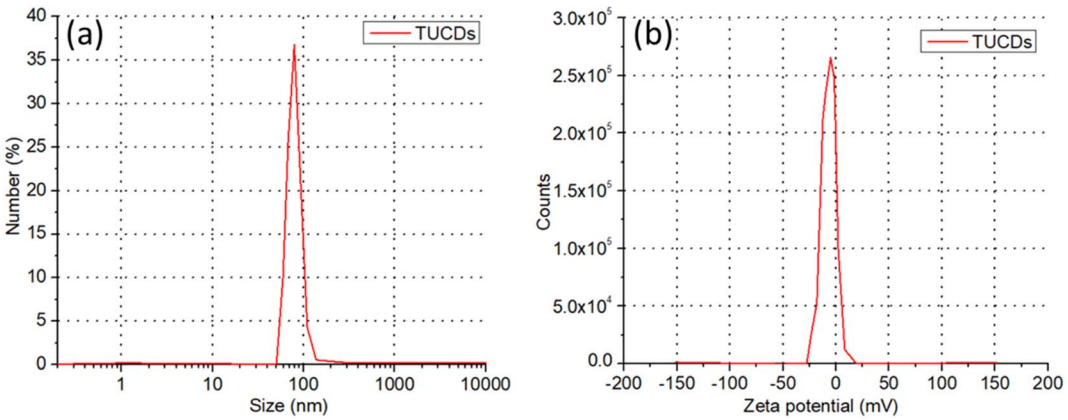

Fig. 4 (a) DLS spectrum of TUCDs in aqueous medium (b) zeta potential measurement of the TUCDs.

incorporation of nitrogen and sulfur dopants, enhancing surface functionalities and improving interactions with negatively charged biological membranes or biomolecules. The combination of narrow size distribution and high zeta potential underscores the potential of TUCDs for stable dispersion in aqueous systems and their application in targeted delivery systems, fluorescence imaging, and biosensing. These findings corroborate the efficient synthesis method and provide a strong foundation for further exploration of TUCDs in advanced functional applications.

Fig. 5 shows the XPS analysis of TUCDs, providing detailed insights into their elemental composition and chemical states. The XPS survey spectrum in Fig. 5(a) confirms the presence of carbon (C 1s), oxygen (O 1s), and nitrogen (N 1s) as the primary elements, consistent with the nitrogen and sulfur co-doping strategy. The high-resolution C 1s spectrum in Fig. 5(b) is deconvoluted into three distinct peaks at approximately 284.8 eV, 286.2 eV, and 288.5 eV, corresponding to C–C, C–N, and C═O/C–O bonds, respectively.[61,62] These peaks highlight the successful incorporation of nitrogen into the carbon framework and the presence of oxygen-containing functional groups, which enhance the hydrophilicity and functional versatility of the TUCDs. Similarly, the high-resolution O 1s spectrum in Fig. 5(c) reveals peaks at 5316 eV and 533.2 eV, attributed to C═O and C–OH/C–O–C bonds, respectively, further corroborating the abundance of oxygen-functionalized groups on the TUCD's surface.[63,64] The N 1s spectrum in Fig. 5(d) displays two peaks centered at 398.4 eV and 400.6 eV, corresponding to pyridinic N and pyrrolic N, respectively, confirming the effective doping of nitrogen into the carbon lattice.[64,65] The presence of pyridinic and pyrrolic nitrogen is particularly significant, as it imparts additional active sites for potential catalytic and biological applications, alongside enhancing the photoluminescent properties of the TUCDs. Collectively, the XPS results not only verify the elemental composition and doping efficacy but also underscore the surface functionality of TUCDs, which is pivotal for their application in biomedicine, sensing, and energy-related technologies. The combination of nitrogen and oxygen functional groups, alongside their precise chemical states, enhances the TUCDs' stability, reactivity, and suitability for advanced multifunctional applications.

Fig. 6 illustrates the antioxidant properties of TUCDs through their radical scavenging activities against DPPH (a), hydroxyl radicals (b), and $KMnO_4$ radicals (c). These results underscore the effectiveness of TUCDs as potent antioxidants. In Fig. 6(a), the DPPH radical scavenging activity exhibits a concentration-dependent trend, with nearly 85% scavenging

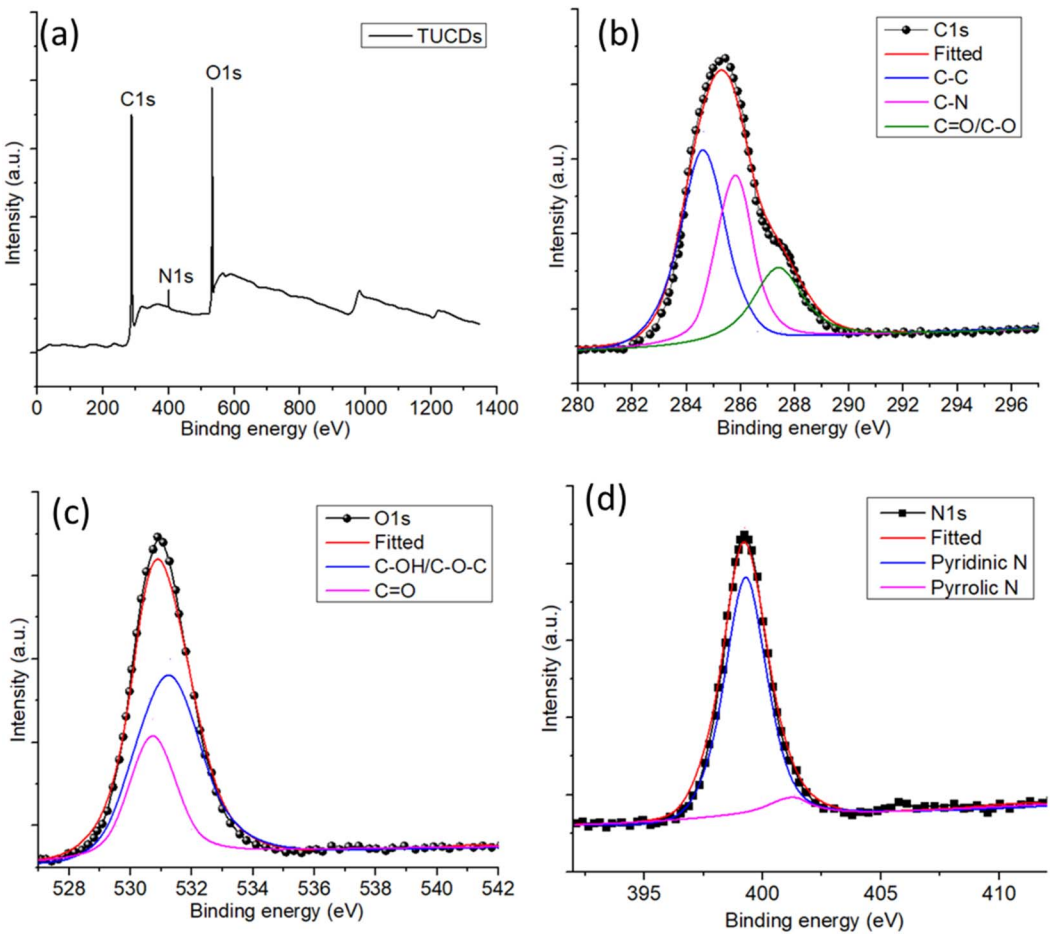

Fig. 5 (a) XPS survey spectrum of the TUCDs. High resolution (b) C 1s (b) O 1s and (d) N 1s spectra of the TUCDs.

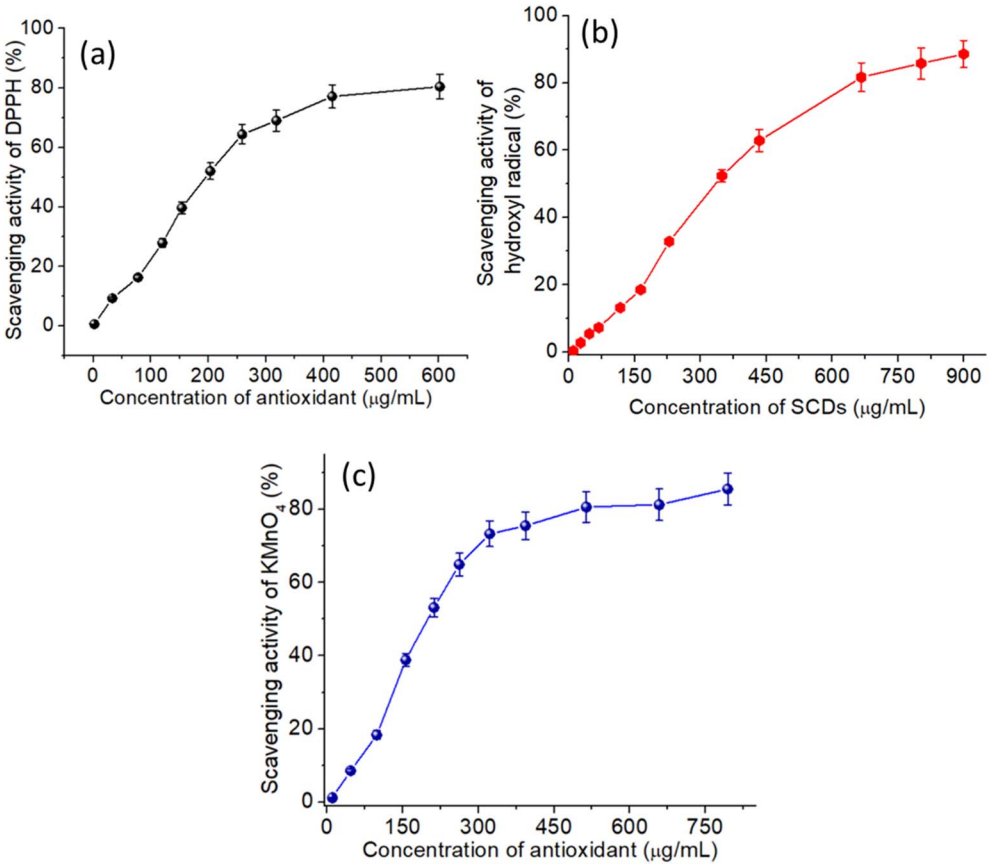

Fig. 6 (a) DPPH radical scavenging activity of the TUCDs (b) hydroxyl radical scavenging activity of the TUCDs (c) $KMnO_4$ radical scavenging activity of the TUCDs.

efficiency achieved at a TUCD concentration of 600 μg mL^{-1}, highlighting their remarkable electron-donating ability to neutralize free radicals. Similarly, Fig. 6(b) shows the hydroxyl radical scavenging activity, where the TUCDs demonstrate a significant radical quenching efficiency, reaching approximately 90% scavenging at a concentration of 900 μg mL^{-1}, attributed to the presence of oxygen-rich functional groups, such as hydroxyl and carboxyl groups, on the surface of TUCDs. These groups provide active sites for radical neutralization. Fig. 6(c) further reveals the TUCDs' scavenging activity against $KMnO_4$ radicals, achieving a plateau of approximately 85% scavenging efficiency at 750 μg mL^{-1}, indicating their capacity to interact with diverse radical species. The superior antioxidant performance of TUCDs can be attributed to their unique structural features and surface chemistry. The co-doping of nitrogen and sulfur introduces additional active sites, such as pyridinic and pyrrolic nitrogen, which enhance the electron transfer and radical stabilization mechanisms. Moreover, the extensive surface area and many oxygen-functional groups of TUCDs facilitate improved interactions with reactive oxygen species (ROS), resulting in effective quenching of free radicals. These attributes render TUCDs especially appropriate for biomedical applications, encompassing ROS-induced damage mitigation, neuroprotection, and therapies connected to oxidative stress. The notable radical scavenging efficiencies found across several radical systems highlight the versatility and effectiveness of TUCDs as multifunctional antioxidants in multiple fields.

The photoluminescence (PL) characteristics of TUCDs in reaction to 3NT were thoroughly examined, as illustrated in Fig. 7(a and b). Fig. 7(a) displays the photoluminescence spectra of TUCDs subjected to escalating amounts of 3NT (0–160 μM). A considerable reduction in PL intensity is noted with increasing 3NT concentrations, signifying effective interaction between TUCDs and 3NT molecules. The quenching is due to energy transfer or electron transfer mechanisms enabled by the nitro group in 3NT, which efficiently absorbs energy from the excited state of TUCDs. This pronounced quenching effect underscores the sensitivity of TUCDs to minimal concentrations of 3NT, indicating their potential as sensors for nitroaromatic chemicals. Fig. 7(b) illustrates the associated Stern–Volmer plot, which correlates the ratio of initial photoluminescence intensity (I_0) to the photoluminescence intensity post-quenching (I) with the concentration of 3NT. The data reveal a linear correlation at lower concentrations, demonstrating dynamic quenching due to collisions between 3NT and TUCDs. At high concentrations, slight deviations from linearity are seen, indicating a potential effect of static quenching, which is defined by the formation of non-emissive ground-state complexes. The Stern–Volmer constant derived from the linear region clarifies

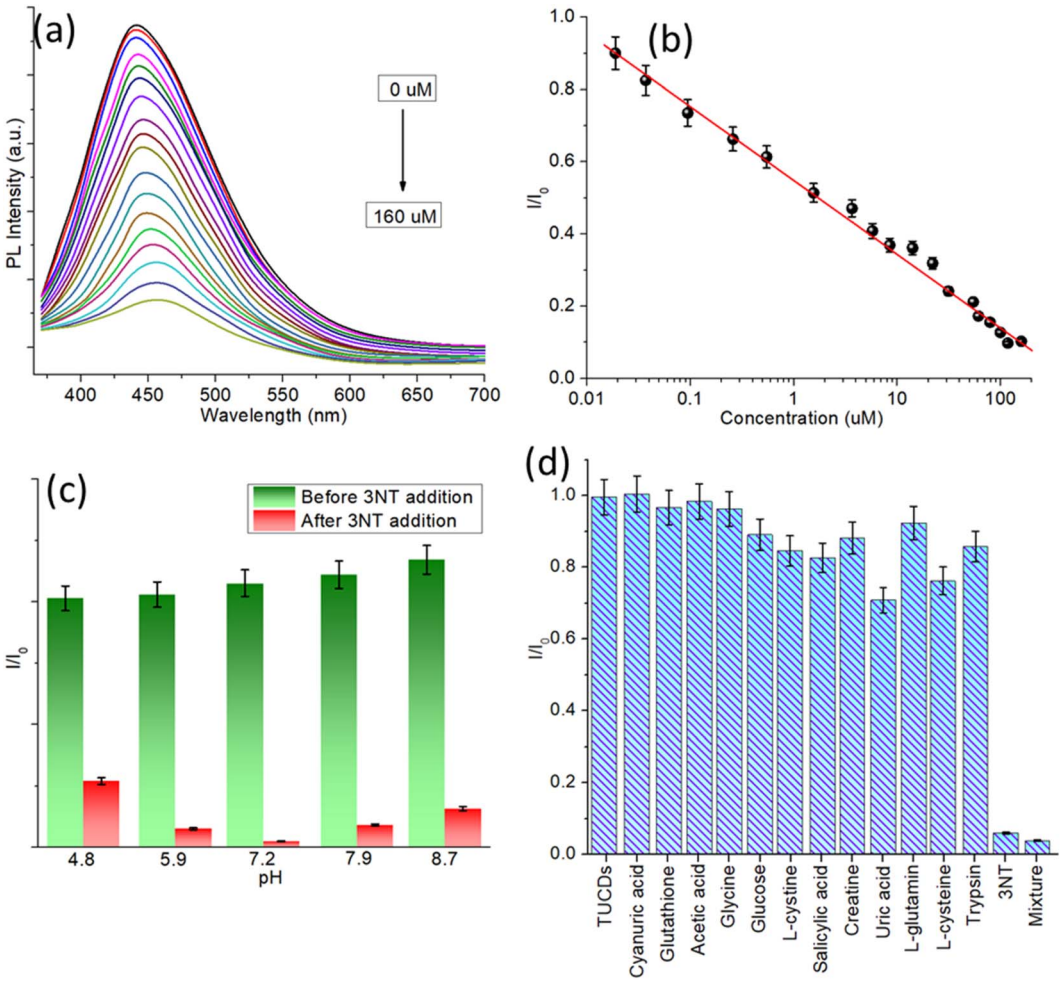

Fig. 7 (a) PL spectra of TUCDs with different concentrations of 3NT (b) change or PL intensity signal with 3NT concentration (c) change or PL intensity signal in different pH with and without 3NT concentration (d) selectivity analysis of TUCDs against different physiological solutions showing fluctuations of PL intensities.

the quenching efficiency and the interaction intensity between TUCDs and 3NT. Fig. 7(c) analyzes the influence of pH on the photoluminescence response of TUCDs prior to and following the addition of 3NT. The PL intensity of TUCDs remained consistently stable across a wide pH range (4.8–8.7), demonstrating their resilience in many environmental circumstances. Nevertheless, the introduction of 3NT results in a marked reduction in PL intensity at all pH levels. This behavior validates the efficacy of the quenching mechanism, demonstrating its independence from pH, and indicating that TUCDs can consistently detect 3NT across various pH conditions, including physiological and environmental samples. The capacity of TUCDs to sustain steady photoluminescence across varying pH settings is essential for their practical utilization. Fig. 7(d) assesses the selectivity of TUCDs for 3NT by analyzing the PL quenching response in the presence of several potentially confounding compounds, such as amino acids, metal ions, and prevalent physiological analytes. The majority of examined interferents exhibit minimal effect on the photoluminescence intensity of TUCDs, indicating their chemical stability and resilience to non-specific interactions. Conversely, 3NT produces a significant quenching effect, underscoring the remarkable selectivity of TUCDs for the detection of 3NT. Significantly, even in the presence of a combination of interferents, the PL quenching by 3NT remains evident, thus underscoring the dependability of TUCDs as a selective probe.

Fig. 8 investigates two critical aspects of the interaction between TUCDs and 3NT: response time and zeta potential changes upon binding. Fig. 8(a) shows the response time of TUCDs to 3NT, characterized by the ratio of initial PL intensity (I_0) to quenched PL intensity (I) over time. The quenching occurs almost instantaneously, with the I_0/I ratio reaching a stable minimum within the first few minutes and remaining constant up to 120 minutes. This rapid response reflects the high reactivity of TUCDs toward 3NT and indicates an efficient quenching mechanism, likely due to strong binding or interaction between TUCDs and 3NT molecules. The near-instantaneous response further underscores the practicality of TUCDs for real-time sensing applications, especially in scenarios requiring fast detection. Fig. 8(b) explores the

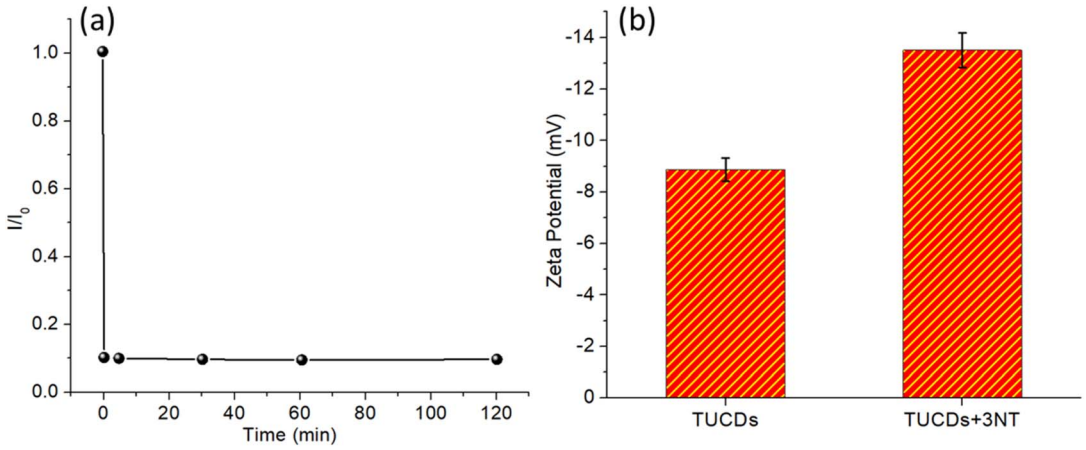

Fig. 8 (a) Determination of response time of TUCDs in presence of 3NT (b) zeta potential values of TUCDs after attachment to 3NT.

changes in zeta potential of TUCDs before and after exposure to 3NT, providing insight into surface interactions. The zeta potential of bare TUCDs is approximately −10 mV, indicative of their negatively charged surface, likely due to the presence of thiol groups or other functional moieties. Upon binding with 3NT, the zeta potential shifts significantly to more negative values, around −14 mV. This shift confirms the adsorption of 3NT onto the surface of TUCDs, which increases the overall surface charge density. The increased negativity may be attributed to the introduction of nitro groups from 3NT, which contribute additional charge upon interaction with TUCDs. These changes in zeta potential further validate the strong interaction between TUCDs and 3NT, which is consistent with the observed quenching behavior.

Table 1 provides a comparative analysis of heteroatom-doped carbon dots (CDs) used for detecting various biomolecules and analytes, benchmarking the performance of our study against existing literature. Our tamarind-derived CDs exhibit pH-dependent sensitivity for detecting 3-nitrotyrosine, a crucial oxidative stress metabolite linked to neurodegenerative

Table 1 Different CDs based nanoprobes for analyte detection in fluorimetric method

Carbon source	Synthesis method	Heteroatom doping	Target analyte	Detection sensitivity	Biomedical application	Ref.
Citric acid and urea	Hydrothermal	Nitrogen and sulfur	Reactive oxygen species (ROS)	Not specified	Theranostic platform for free radical scavenging, imaging, and chemotherapy	66
Citric acid and phosphoric acid	Hydrothermal	Phosphorus	Fe^{3+} ions	Detection limit of 0.33 μM	Potential applications in sensing and bioimaging	67
Citric acid and thiourea	Hydrothermal	Nitrogen and sulfur	Fe^{3+} ions and L-cysteine	Detection limits of 0.16 μM (Fe^{3+}) and 0.12 μM (L-cysteine)	Detection in real samples and colon cancer cell imaging	68
Aminosalicylic acid	Hydrothermal	Nitrogen	Fe^{3+} ions and tetracycline	Detection limit of 0.1 μM (Fe^{3+}) and 0.05 μM (tetracycline)	Potential applications in environmental monitoring and pharmaceutical analysis	69
Citric acid and ethylenediamine	Hydrothermal	Nitrogen	Picric acid	Detection limit of 0.23 μM	Potential applications in environmental safety and explosive detection	70
Medicinal plants	Hydrothermal	Nitrogen and sulfur	Fe^{3+} ions	Detection limit of 0.27 μM	Applications in bioimaging and Fe^{3+} detection	71
Citric acid and thiourea	Hydrothermal	Nitrogen and sulfur	Dopamine	Detection limit of 0.15 μM	Potential applications in neurological disorder diagnostics	72
Citric acid and urea	Hydrothermal	Nitrogen	Ascorbic acid	Detection limit of 0.2 μM	Applications in food safety and quality control	73
Citric acid and ethylenediamine	Hydrothermal	Nitrogen	Glutathione	Detection limit of 0.18 μM	Potential applications in oxidative stress monitoring and disease diagnostics	74
Tamarind	One-step hydrothermal	Nitrogen	3-Nitrotyrosine	pH-Dependent sensitivity (pH 4.8–8.7)	Detection of oxidative stress metabolites associated with neurodegenerative diseases	This study

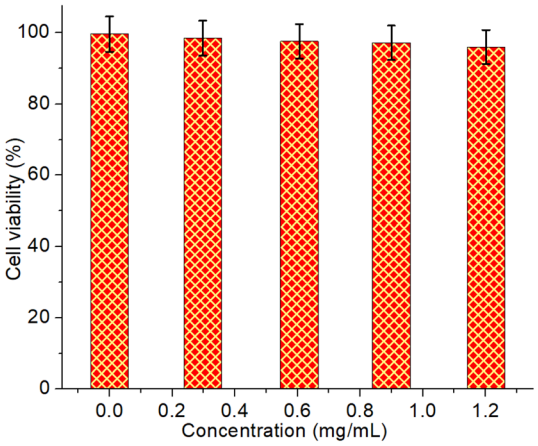

Fig. 9 Cytotoxicity assay of the TUCDs (aqueous dispersion) against fibroblasts 3T3 cell lines.

diseases, distinguishing them from other reported CDs. Compared to previous studies that primarily target Fe^{3+} ions, dopamine, and reactive oxygen species (ROS), our work uniquely focuses on a metabolite directly relevant to oxidative stress-related disorders. Additionally, the sustainable and cost-effective synthesis route using tamarind as a carbon source enhances the environmental viability of our approach. The table also highlights the diverse biomedical applications of CDs, ranging from neurodiagnostics and bioimaging to pharmaceutical and environmental monitoring. These comparisons emphasize the novelty of our study in bridging sustainable nanomaterials with practical healthcare applications.

Fig. 9 illustrates the cytotoxicity assessment of TUCDs in aqueous dispersion against 3T3 fibroblast cell lines, providing insights into their biocompatibility. The cell viability was measured after exposure to various concentrations of TUCDs ranging from 0.2 mg mL^{-1} to 1.2 mg mL^{-1}. Across all tested concentrations, the cell viability remains consistently high, exceeding 95% in all cases, and is statistically similar to the control group (0.0 mg mL^{-1}). This result strongly suggests that TUCDs exhibit negligible cytotoxicity under these experimental conditions, even at the highest concentration tested. The lack of significant toxicity can be attributed to the surface chemistry of the TUCDs, which likely minimizes adverse interactions with cellular components. The stability of the nanoparticles in aqueous dispersion and their minimal leaching of toxic ions or reactive species further enhance their safety profile. This excellent biocompatibility indicates that TUCDs are well-suited for applications involving biological systems, such as biosensing, bioimaging, and environmental monitoring.

4. Conclusions

This study presents a sustainable and cost-effective approach for synthesizing heteroatom-doped carbon dots from tamarind, leveraging a one-step hydrothermal method. The successful incorporation of nitrogen dopants into the carbon framework enhances their physicochemical properties, making them suitable for a range of biomedical applications. Advanced spectroscopic analyses confirmed their structural integrity and functional attributes, highlighting their stability and tunable fluorescence properties. A key highlight of this study is the exceptional antioxidant activity of the synthesized CDs, demonstrated by their robust free-radical scavenging efficiency exceeding 80% across multiple assay techniques. This strong antioxidant capability suggests their potential in mitigating oxidative stress, a key factor in various pathological conditions, including neurodegenerative disorders. Additionally, their remarkable selectivity and sensitivity in detecting oxidative stress metabolites, particularly 3-nitrotyrosine, further underscore their diagnostic utility. The detection efficiency was found to be pH-dependent, offering a versatile sensing mechanism adaptable to different physiological environments. Biocompatibility assessments with fibroblast cells validated the non-toxic nature of these CDs, reinforcing their suitability for biomedical applications. Their ability to function as a rapid and highly selective probe for oxidative stress biomarkers positions them as a promising tool for early disease detection, particularly in neurodegenerative disorders where oxidative damage plays a crucial role. This research illustrates the promise of tamarind-derived heteroatom-doped carbon dots as multifunctional nanomaterials that connect sustainable material design with practical therapeutic applications. Their amalgamation of antioxidant effectiveness, biocompatibility, and diagnostic sensitivity positions them as a significant platform for medicinal and biosensing applications. Subsequent study may investigate their incorporation into sophisticated biosensors or precise drug delivery mechanisms, so enhancing their influence in biomedical and clinical investigations. At the same time, it is possible to guide the decisive factors for carbon dots employing artificial intelligence techniques to synthesize the desired CDs and assess disease signature pathways of neurodegenerative and metabolic disorders through oxidative stress pathways.

Data availability

The data that support the findings of this study are available on request from the corresponding author.

Author contributions

Mohammad Tabish, and Mohd Afzal: scientific and technical discussion, Abdulrahman M. Alshahrani and Iram Malik: formal analysis, investigation, and interpretation of data. Mohd Afzal: data curation, formal analysis, investigation, writing review, and editing. Iram Malik: substantial contribution to conceptualization, methodology, drafting, designing, acquisition, analysis, interpretation of data, and writing – review and editing the article.

Conflicts of interest

There are no conflicts to declare.

Acknowledgements

The authors extend their appreciation to the King Salman Center for Disability Research for funding this work through Research Group no. KSRG-2024-041.

References

1 D. C. Bergen and D. Silberberg, *Arch. Neurol.*, 2002, **59**, 1194.
2 B. Uttara, A. Singh, P. Zamboni and R. Mahajan, *Curr. Neuropharmacol.*, 2009, **7**, 65–74.
3 U. C. Dash, N. K. Bhol, S. K. Swain, R. R. Samal, P. K. Nayak, V. Raina, S. K. Panda, R. G. Kerry, A. K. Duttaroy and A. B. Jena, *Acta Pharm. Sin. B*, 2025, **15**, 15–34.
4 J. Li, W. O, W. Li, Z.-G. Jiang and H. Ghanbari, *Int. J. Mol. Sci.*, 2013, **14**, 24438–24475.
5 M. Ramalingam and S.-J. Kim, *J. Neural Transm.*, 2012, **119**, 891–910.
6 S. Shohag, S. Akhter, S. Islam, T. Sarker, M. K. Sifat, M. M. Rahman, M. R. Islam and R. Sharma, *Oxid. Med. Cell. Longevity*, 2022, **2022**, 1–20.
7 O. E. Oke, O. A. Akosile, A. I. Oni, I. O. Opowoye, C. A. Ishola, J. O. Adebiyi, A. J. Odeyemi, B. Adjei-Mensah, V. A. Uyanga and M. O. Abioja, *Poult. Sci.*, 2024, **103**, 104003.
8 D. F. Santos, S. Simão, C. Nóbrega, J. Bragança, P. Castelo-Branco and I. M. Araújo, *FEBS Lett.*, 2024, **598**, 2074–2091.
9 K. Renu, A. V. Gopalakrishnan and H. Madhyastha, *Odontology*, 2024, DOI: 10.1007/s10266-024-01032-x.
10 M. M. Rahman, M. R. Islam, S. Akash, M. Harun-Or-Rashid, T. K. Ray, M. S. Rahaman, M. Islam, F. Anika, M. K. Hosain, F. I. Aovi, H. A. Hemeg, A. Rauf and P. Wilairatana, *Biomed. Pharmacother.*, 2022, **153**, 113305.
11 E. Maser, *Biochem. Biophys. Res. Commun.*, 2006, **340**, 1019–1022.
12 R. Ullah, M. Khan, S. A. Shah, K. Saeed and M. O. Kim, *Nutrients*, 2019, **11**, 1195.
13 A. Tassone, M. Meringolo, G. Ponterio, P. Bonsi, T. Schirinzi and G. Martella, *Int. J. Mol. Sci.*, 2023, **24**, 7221.
14 K. J. Barnham and A. I. Bush, *Chem. Soc. Rev.*, 2014, **43**, 6727–6749.
15 S. Nangare and P. Patil, *Crit. Rev. Anal. Chem.*, 2022, **52**, 1139–1169.
16 A. Saravanan, P. Das, M. Maruthapandi, S. Aryal, S. Michaeli, Y. Mastai, J. H. T. Luong and A. Gedanken, *Surf. Interfaces*, 2024, **46**, 103857.
17 P. Das, M. Maruthapandi, A. Saravanan, M. Natan, G. Jacobi, E. Banin and A. Gedanken, *ACS Appl. Nano Mater.*, 2020, **3**, 11777–11790.
18 P. Das, S. Ganguly, P. K. Marvi, M. Sherazee, X. (Shirley) Tang, S. Srinivasan and A. R. Rajabzadeh, *Adv. Mater.*, 2024, **36**, 2409819.
19 H. Liu, X. Zhong, Q. Pan, Y. Zhang, W. Deng, G. Zou, H. Hou and X. Ji, *Coord. Chem. Rev.*, 2024, **498**, 215468.
20 D. Ozyurt, M. Al Kobaisi, R. K. Hocking and B. Fox, *Carbon Trends*, 2023, **12**, 100276.
21 Z. Yu, F. Li and Q. Xiang, *J. Mater. Sci. Technol.*, 2024, **175**, 244–257.
22 S. Ganguly, P. Das, E. Itzhaki, E. Hadad, A. Gedanken and S. Margel, *ACS Appl. Mater. Interfaces*, 2020, **12**, 51940–51951.
23 P. Das, S. Ganguly, S. Margel and A. Gedanken, *Nanoscale Adv.*, 2021, **3**, 6762–6796.
24 R. Subash, K. Madhivanan, R. Atchudan, S. Arya and A. K. Sundramoorthy, *Diamond Relat. Mater.*, 2025, **152**, 111940.
25 A. Dubey, A. Ahmed, A. Singh, A. K. Sundramoorthy and S. Arya, *Diamond Relat. Mater.*, 2024, **149**, 111596.
26 M. Thakur, A. Singh, A. Dubey, A. K. Sundramoorthy, P. Kumar and S. Arya, *Emergent Mater.*, 2024, **7**, 1805–1817.
27 S. Ganguly and S. Margel, *Talanta Open*, 2023, **8**, 100243.
28 A. Dubey, A. Singh, A. K. Sundramoorthy, S. Dixit, N. I. Vatin, M. ud D. Rather and S. Arya, *J. Environ. Chem. Eng.*, 2025, **13**, 115155.
29 A. Singh, S. S. Shah, C. Sharma, V. Gupta, A. K. Sundramoorthy, P. Kumar and S. Arya, *J. Environ. Chem. Eng.*, 2024, **12**, 113032.
30 P. Singh, S. K. Arpita, P. Kumar, N. Kataria, V. Bhankar, K. Kumar, R. Kumar, C.-T. Hsieh and K. S. Khoo, *Nanoscale*, 2023, **15**, 16241–16267.
31 X. Sun and Y. Lei, *TrAC, Trends Anal. Chem.*, 2017, **89**, 163–180.
32 P. Das, S. Ganguly, A. Saha, M. Noked, S. Margel and A. Gedanken, *ACS Appl. Mater. Interfaces*, 2021, **13**, 31038–31050.
33 P. Das, S. Ganguly, S. Margel and A. Gedanken, *Langmuir*, 2021, **37**, 3508–3520.
34 P. Das, S. Ganguly, A. Saravanan, S. Margel, A. Gedanken, S. Srinivasan and A. R. Rajabzadeh, *ACS Appl. Bio Mater.*, 2022, **5**, 5617–5633.
35 S. Anwar, H. Ding, M. Xu, X. Hu, Z. Li, J. Wang, L. Liu, L. Jiang, D. Wang, C. Dong, M. Yan, Q. Wang and H. Bi, *ACS Appl. Bio Mater.*, 2019, **2**, 2317–2338.
36 M. S. Alkaltham, S. A. Althawab, T. Alsulami and A. Alzahrani, *Diamond Relat. Mater.*, 2024, **149**, 111624.
37 S. K. Beura, A. R. Panigrahi, P. Yadav, I. Palacio, E. Casero, C. Quintana, J. Singh, M. K. Singh, J. A. Martín Gago and S. K. Singh, *Ageing Res. Rev.*, 2024, **94**, 102205.
38 S. I. Anjo, Z. He, Z. Hussain, A. Farooq, A. McIntyre, C. A. Laughton, A. N. Carvalho and M. J. Finelli, *Antioxidants*, 2024, **13**, 681.
39 E. L. Que, D. W. Domaille and C. J. Chang, *Chem. Rev.*, 2008, **108**, 1517–1549.
40 G. S. Wilson and M. A. Johnson, *Chem. Rev.*, 2008, **108**, 2462–2481.
41 M. S. García-Gutiérrez, F. Navarrete, F. Sala, A. Gasparyan, A. Austrich-Olivares and J. Manzanares, *Front. Psychiatry*, 2020, **11**, 432.
42 X. Y. Wong, A. Sena-Torralba, R. Álvarez-Diduk, K. Muthoosamy and A. Merkoçi, *ACS Nano*, 2020, **14**, 2585–2627.
43 D. Brambilla, B. Le Droumaguet, J. Nicolas, S. H. Hashemi, L.-P. Wu, S. M. Moghimi, P. Couvreur and K. Andrieux, *Nanomed.: Nanotechnol. Biol. Med.*, 2011, **7**, 521–540.

44 A. Bandyopadhyay, T. Das, S. Nandy, S. Sahib, S. Preetam, A. V. Gopalakrishnan, A. Dey and N. Schmiedebergs, *Arch. Pharmacol.*, 2023, **396**, 3417–3441.
45 W. Deng, C. Zang, Q. Li, B. Sun, X. Mei, L. Bai, X. Shang, Y. Deng, Y. Xiao, R. A. Ghiladi, G. H. Lorimer, X. Zhang and J. Wang, *ACS Biomater. Sci. Eng.*, 2023, **9**, 1307–1319.
46 S. Chen, R. Li, Y. Liu, Z. Zhang, M. Fang, S. Huang, Y. Li and L. Geng, *Langmuir*, 2024, **40**, 26018–26025.
47 A. Bhaloo, S. Nguyen, B. H. Lee, A. Valimukhametova, R. Gonzalez-Rodriguez, O. Sottile, A. Dorsky and A. V. Naumov, *Antioxidants*, 2023, **12**, 1536.
48 H. Ding, J.-S. Wei and H.-M. Xiong, *Nanoscale*, 2014, **6**, 13817–13823.
49 H. Xu, X. Yang, G. Li, C. Zhao and X. Liao, *J. Agric. Food Chem.*, 2015, **63**, 6707–6714.
50 P. Das, S. Ganguly, P. P. Maity, H. K. Srivastava, M. Bose, S. Dhara, S. Bandyopadhyay, A. K. Das, S. Banerjee and N. C. Das, *J. Photochem. Photobiol., B*, 2019, **197**, 111545.
51 A. Khan, P. Ezati and J.-W. Rhim, *ACS Appl. Bio Mater.*, 2023, **6**, 1294–1305.
52 B. S. B. Kasibabu, S. L. D'souza, S. Jha and S. K. Kailasa, *J. Fluoresc.*, 2015, **25**, 803–810.
53 P. Das, S. Ganguly, S. R. Ahmed, M. Sherazee, S. Margel, A. Gedanken, S. Srinivasan and A. R. Rajabzadeh, *ACS Appl. Polym. Mater.*, 2022, **4**, 9323–9340.
54 P. Das, M. Sherazee, P. K. Marvi, S. R. Ahmed, A. Gedanken, S. Srinivasan and A. R. Rajabzadeh, *ACS Appl. Mater. Interfaces*, 2023, **15**, 29425–29439.
55 S. Ganguly, P. Das, S. Das, U. Ghorai, M. Bose, S. Ghosh, M. Mondal, A. K. Das, S. Banerjee and N. C. Das, *Colloids Surf., A*, 2019, **579**, 123604.
56 P. Das, S. Ganguly, P. K. Marvi, S. Hassan, M. Sherazee, M. Mahana, X. (Shirley) Tang, S. Srinivasan and A. R. Rajabzadeh, *Adv. Healthcare Mater.*, 2025, **14**, 2404911.
57 Y. Zhou, W. Zhang and R. M. Leblanc, *J. Phys. Chem. B*, 2022, **126**, 10777–10796.
58 S. Ganguly, P. Das, S. Banerjee and N. C. Das, *Funct. Compos. Struct.*, 2019, **1**, 022001.
59 P. Das, S. Ganguly, S. Banerjee and N. C. Das, *Res. Chem. Intermed.*, 2019, **45**, 3823–3853.
60 A. Öztürk and A. Bayrakçeken Yurtcan, *J. Solid State Chem.*, 2021, **296**, 121972.
61 D. Li, S. Wang, F. Azad, L. Zhao and S. Su, *Microchim. Acta*, 2019, **186**, 612.
62 Q. Niu, K. Gao, Z. Lin and W. Wu, *Anal. Methods*, 2013, **5**, 6228.
63 M. Sevilla and A. B. Fuertes, *Chem.–A Eur. J.*, 2009, **15**, 4195–4203.
64 M. Vedamalai, A. P. Periasamy, C.-W. Wang, Y.-T. Tseng, L.-C. Ho, C.-C. Shih and H.-T. Chang, *Nanoscale*, 2014, **6**, 13119–13125.
65 X.-J. Jin, M.-Y. Zhang, Y. Wu, J. Zhang and J. Mu, *Ind. Crops Prod.*, 2013, **43**, 617–622.
66 K. Dehvari, S.-H. Chiu, J.-S. Lin, W. M. Girma, Y.-C. Ling and J.-Y. Chang, *Acta Biomater.*, 2020, **114**, 343–357.
67 G. Kalaiyarasan, J. Joseph and P. Kumar, *ACS Omega*, 2020, **5**, 22278–22288.
68 R. Tamizhselvi, K. S. Velu, A. A. Napoleon, M. S. Akhtar, N. Ahmad, S. Palanisamy, S. You, S. Mohandoss and S.-C. Kim, *Inorg. Chem. Commun.*, 2025, **172**, 113662.
69 Y. Song, C. Zhu, J. Song, H. Li, D. Du and Y. Lin, *ACS Appl. Mater. Interfaces*, 2017, **9**, 7399–7405.
70 J. Vinoth Kumar, G. Kavitha, R. Arulmozhi, V. Arul, S. Singaravadivel and N. Abirami, *J. Fluoresc.*, 2021, **31**, 915–932.
71 S. Kota, P. Dumpala, R. Sajja and R. Anantha, *Sci. Rep.*, 2024, **14**, 13160.
72 G. Balkourani, A. Brouzgou and P. Tsiakaras, *Carbon N. Y.*, 2023, **213**, 118281.
73 Y. Liu, M. Zhao and Q. Zhu, *J. Fluoresc.*, 2023, **33**, 2391–2401.
74 W.-J. Niu, Y. Li, R.-H. Zhu, D. Shan, Y.-R. Fan and X.-J. Zhang, *Sens. Actuators, B*, 2015, **218**, 229–236.